WORLD CONFERENCE ON TIMBER ENGINEERING 2025
BRISBANE, AUSTRALIA
Advancing Timber for the Future Built Environment

UNCERTAINTY QUANTIFICATION OF FOUR PHENOMENOLOGICAL HYSTERETIC TIMBER MODELS

Matías F. Chacón[1], Pablo Guindos[2]

ABSTRACT: This article evaluates the uncertainty associated with four phenomenological-based hysteretic timber models from the literature: SAWS/MSTEW, DowelType, modified Richard–Abbott, and ASPID. These models can simulate various timber connections and assemblies, addressing behaviors such as pinching, symmetry and asymmetry, strength and stiffness degradation, and low-cycle fatigue. The models were validated against four experimental benchmark timber tests using an optimized parameter identification process for all cases. The study compared the strength capacity, peak displacement, and energy dissipation. Furthermore, three goodness-of-fit metrics were assessed for the force and energy dissipation histories: Normalized Root Mean Square (NRMS) error, Normalized Mean Absolute (NMA) error, and the coefficient of determination R^2. Numerical results indicated that all models, except the SAWS model, achieved good strength capacity and total dissipated energy accuracy, with errors of less than 7%. The models also demonstrated a good fit over time, with NRMS and NMA errors of less than 8.54% for the force history and 4.4% for the dissipated energy history, and R^2 values that exceeded 83.11% and 97.9% for force and dissipated energy history, respectively. Therefore, in almost all models, the energy dissipation history fits better than the force one.

KEYWORDS: hysteretic timber model, phenomenological-based model, benchmark timber tests, parameter identification, epistemic uncertainty

1 – INTRODUCTION

1.1 OVERVIEW

The hysteresis of connections plays a significant role in the performance of timber structures [9, 30]. It is crucial to utilize accurate nonlinear connection models to ensure reliable designs and predictions for these structures. The characterization of hysteresis in timber members depends on the behavior of their components [27]: (i) wood, which is a quasi-fragile material that tends to crush under tensile, shear, or bending loads; (ii) steel fasteners, which provide considerable strength and ductility; and (iii) the interaction among parts, influenced by factors such as friction and especially the pinching effect, i.e., embedding of wood and the clearance of fasteners, which can result in a sudden drop in strength and stiffness. Fig. 1 illustrates the typical force–displacement $F(u)$ hysteresis of timber members, highlighting the hardening and softening of the envelopes. It also marks pinching during the Unloading–Reloading (UR) paths, stiffness/strength degradation, and low-cycle fatigue phenomenon (i.e., degradation under repetitive cycles of the same amplitude). The UR paths are characterized by three phases based on stiffness variation —i.e., unloading (notable stiffness drop), pinching (quasi-constant stiffness), and reloading (stiffness recovery). Various experimental tests support these observations, including studies on Light-Frame Timber (LFT) walls [23] and Cross-Laminated Timber (CLT) members (e.g., joints [15, 17], walls [13], and slabs [30]).

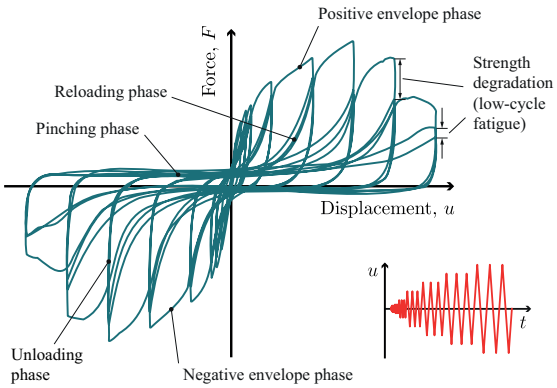

Figure 1: *Typical experimental force–displacement $F(u)$ hysteresis of timber members. This response relates to a half-lapped CLT joint subjected to cyclic in-plane shear load, as tested by Gavrić et al. [15]. The figure is adapted from Chacón & Guindos 2023 [4].*

Moreover, certain connection types demonstrate a quasi-symmetric response when subjected to Positive/Negative

[1] Matías F. Chacón, Centro Nacional de Excelencia para la Industria de la Madera (CENAMAD), Pontificia Universidad Católica de Chile (PUC), Santiago, Chile & Department of Structural and Geotechnical Engineering, PUC, mfchacon@uc.cl

[2] Pablo Guindos, CENAMAD & Faculty of Architecture and Centro de Innovación Tecnolóxica en Edificación e Enxeñería Civil (CITEEC), Universidade da Coruña, A Coruña, Spain, pablo.guindos@udc.es

https://doi.org/10.52202/080513-0179

(P/N) loads, such as traditional screwed, nailed, and bolted connections. In contrast, other scenarios exhibit a different kind of asymmetry, which can be categorized as follows: (i) displacement — observed in components that experience combined lateral and axial loads [23]; (ii) force — seen in hybrid timber-stiffer material joints [3]; and (iii) taxonomic differences, which refer to varying tensile and compressive behaviors, as found in anchorage systems like hold-downs, steel angle brackets, and anchor tie-downs [14].

1.2 HYSTERETIC TIMBER MODELS

Several hysteretic timber models are proposed in the literature, which can be classified into three main groups: (i) detailed micro-models, where each material is simulated individually using 3D solid and/or contact finite elements along with a mechanical approach [19]; (ii) component macro-models, where each component, such as fasteners, anchors, sheathing/CLT panels, and/or frame, is modeled separately with nonlinear coupled/uncoupled springs and/or shells elements combined with mechanical or phenomenological formulations (e.g., LFT walls [8], CLT walls [16], and CLT slabs [2]); and (iii) simplified macro-models, where the entire member is represented by a set of uncoupled/coupled uniaxial Single Degree-Of-Freedom (SDOF) nonlinear springs with a phenomenological approach (e.g., LFT walls [25] and CLT walls [18]). Among these approaches, phenomenological models offer a favorable balance between accuracy and computational efficiency for simulating planar members and assemblies.

Various phenomenological-based hysteretic timber models are documented in the literature, differing in the type of constitutive equations (e.g., algebraic [29], transcendental [1], and first-order Ordinary Differential Equations (ODE)s [26] or in the shape of the UR paths (e.g., smooth [4, 7, 11, 22, 25] and polygonal [10]). All these models simulate the UR paths and pinching effect with varying degrees of accuracy. Moreover, some models also incorporate stiffness and strength degradation through different methods, such as Displacement (D)-based [24], Energy (E)-based (which include considerations for low-cycle fatigue) [9], and Energy-Displacement (ED)-based approaches [4, 5, 7, 26]. Furthermore, several models address the asymmetry between positive and negative cycles in their hysteresis using various methods. These include employing two distinct envelopes and UR paths for each loading direction, adding terms to the ODEs, utilizing P/N independent damage variables, or implementing a set of parallel springs [4, 5, 7].

1.3 OBJECTIVE AND METHODOLOGY

This article compares the hysteresis uncertainty among four phenomenological-based timber models by validating them against four experimental timber benchmarks. The paper is structured as follows: Section 2 provides a brief overview of the four models studied. The validation of these models using four experimental benchmark tests is presented in Section 3. Conclusions are drawn in Section 4. Finally, Appendix A lists all the optimized parameters for each model and benchmark.

2 – DESCRIPTION OF HYSTERETIC TIMBER MODELS

This section provides a brief description and comparison of the following four hysteretic timber models: (i) Modified Stewart (MSTEW) or SAWS [29]; (ii) DowelType of Dong et al. [7]; (iii) Modified Richard–Abbott (MRA) of Chacón et al. [5]; and (iv) ASymmetrical PInching Degraded (ASPID) of Chacón et al. [4]. The first two models are available in the OpenSees software [20], while the remaining models can be downloaded as Python routines for free.

2.1 MODIFIED STEWART OR SAWS MODEL

This model was initially proposed by Stewart [29] and subsequently modified by Folz & Filiatrault [10]. With only ten parameters, it has the fewest among the studied models, making it widely used for simulating timber connections. The main characteristics of the model are: (i) an exponential envelope based on Foschi et al. [11]; (ii) polygonal UR paths; (iii) symmetrical P/N behavior with a single envelope, which in cases of asymmetry, averaged parameters from the P/N fitted envelopes are used; (iv) stiffness degradation during the reloading phase, which is determined by the current maximum absolute displacement (i.e., D-based approach); and (v) strength degradation at the target displacement, which also follows a D-based approach.

2.2 DOWELTYPE MODEL

This model was proposed by Dong et al. [7] and features 11 hysteretic parameters, along with 6 to 20 envelope ones. Its key features are as follows: (i) four types of envelopes (linear piecewise, cubic piecewise, exponential, and cubic Bézier), with only one selected for both P/N directions; (ii) nonlinear smooth UR paths created using a cubic Bézier polynomial for the unloading and reloading phases, and a linear segment for the pinching phase; (iii) can represent both symmetrical and asymmetrical P/N behavior by employing two different sets of parameters for the envelopes and a unique set of ED-based degraded parameters to account for the asymmetry of the UR paths; (iv) stiffness degradation during the reloading, pinching, and unloading phases, along with a D-based strength degradation of the pinching ordinate; and (v) strength degradation at the target displacement with a mixed ED-based approach, while the degradation of the pinching ordinate follows a D-based approach.

2.3 MODIFIED RICHARD–ABBOTT (MRA) MODEL

This model was initially introduced by Richard & Abbott [28] and later modified by Nogueiro et al. [22]. Originally designed to simulate bolted steel connections, the authors discovered that it could also accurately predict the hysteretic behavior of timber connections. This versatility arises from the model's incorporation of various phenomena relevant to these types of joints, including pinching, symmetric and asymmetric P/N behavior, and degradation of strength and stiffness. The latest modified version of the model is utilized in this work. Please refer to [5] for

further details. The main features of this model include: (i) simulates the envelopes and UR paths with a single algebraic function, without the need for loading rules or branches; (ii) nonlinear smooth P/N envelope curves that exhibit both hardening and softening; (iii) management of asymmetry in the envelopes and UR paths using two different sets of parameters; and (iv) degradation of stiffness and strength based on an ED-based approach related to low-cycle fatigue.

2.4 ASYMMETRICAL PINCHING DEGRADED (ASPID) MODEL

This high-fidelity model, recently proposed by the authors [4], is designed to simulate various timber joints, including CLT connections, LFT walls, and anchoring systems, with symmetric and asymmetric behavior. The model comprises 24 physical and graphical parameters, facilitating straightforward calibration against experimental tests. Its key features include: (i) four envelope types (linear piecewise, monotone smooth cubic piecewise [12], exponential-linear, and exponential-cubic), with the option to choose a different type for each direction; (ii) nonlinear smooth UR paths created using a quadratic Bézier polynomial for the unloading and reloading phases, and a linear segment for the pinching phase; (iii) a transition phase between the UR path and the envelope for displacement larger than previous cycles, represented by a smooth quadratic Bézier curve; (iv) asymmetry in envelopes and UR paths

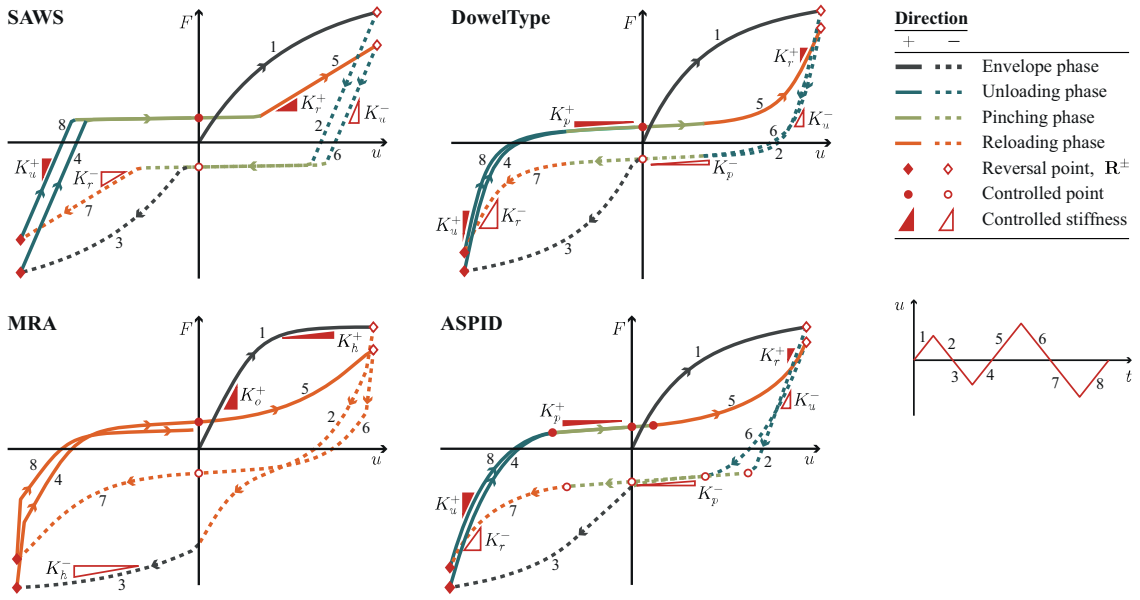

Figure 2: *Schematic description of the four hysteretic timber models. Figure adapted from [6].*

Table 1: *Main properties of the four hysteretic models.*

Property	SAWS	DowelType	MRA	ASPID
Shape				
Envelopes	Exponential [11]	Linear piecewise Cubic Bézier Exponential [11]	Bilinear-exponential	Linear piecewise Cubic piecewise [12] Exponential-linear Exponential-cubic poly
UR phase	Linear	Cubic Bézier	Nonlinear	Quadratic Bézier
Pinching phase	Linear	Linear	Nonlinear	Linear
Asymmetry				
Envelopes	×	✓	✓	✓
Hysteresis	×	✓	✓	✓
Degradation				
Stiffness	$K_r(u_{\max})$	$K_p(u_{\max})$, $K_r(u_{\max})$, $K_u(u_{\max})$	$K_h(u_{\max})$[a]	$K_p(u_{\max})$, $K_r(u_{\max})$
Strength at target disp.	D-based	ED-based	ED-based	ED-based
Strength at null force	Fixed	D-based	Variable[b]	D-based
Low-cycle fatigue	×	×	✓	✓
Cardinality				
Parameters	10	11	36 (=7×4+3×2+2)	22 (=10×2+2)
Envelopes	1	2	2	2

[a] Controls the complete UR path and their stiffnesses (i.e., K_p, K_r, and K_u).

[b] Vary according to the evolution of the primary analytical function.

https://doi.org/10.52202/080513-0179

managed through two distinct sets of parameters and two different types of envelopes; (v) stiffness degradation during reloading, pinching, and unloading stiffness controlled via a D-based approach; and (vi) strength degradation at target displacement addressed with a mixed ED-based approach (for low-cycle fatigue) that employs a novel evolution law, while the pinching ordinate can also degrade with a D-based approach.

2.5 SUMMARY OF MODELS

Fig. 2 schematizes the force–displacement $F(u)$ hysteresis for the four models studied, showing two cycles with increasing amplitude. Moreover, Table 1 summarizes the key features of the models, including their envelope shape, UR path shape, symmetric/asymmetric behavior of the envelope and hysteresis, stiffness and strength degradation, and low-cycle fatigue phenomenon.

3 – VALIDATION OF MODELS

This section details the validation process for the four models of Section 2. It includes four experimental benchmarks of mass timber and lightweight timber connections and assemblies, focusing on both symmetric and asymmetric behavior.

3.1 EXPERIMENTAL BENCHMARK TESTS

The benchmarks consist of various timber connections and members, described as follows: (i) specimen S1 is an in-plane shear CLT joint that displays quasi-symmetrical force/displacement behavior, showing minor differences in both directions; (ii) specimen S2 is an LFT wall subjected to a combination of axial and lateral loads, it has similar strength in both directions but experiences larger negative displacements compared to positive ones; (iii) specimen S3 is a hybrid timber-concrete connection that exhibits comparable displacements in both directions, however, it has significant differences in strength, with the positive force being double that of the opposing force due to the rope effect; and (iv) specimen S4 is a hold-down CLT connection subjected to in-plane axial load, it only demonstrates positive hysteretic behavior (uplift), while the behavior under negative loads (compression of wood) remains uncertain, appearing quasi-linear. Table 2 summarizes the main characteristics of each test specimen. Only specimen S1 shows symmetric behavior, while the others exhibit varying degrees of pronounced asymmetry.

3.2 PARAMETER IDENTIFICATION

An SDOF model was created for each test to generate the hysteresis of all models. A displacement-driven load identical to that used in the experiments was applied. For the SAWS and DowelType models, a two-node zero-length element from the OpenSees software was utilized. In contrast, for MRA and ASPID models, force updating algorithms from the works of [4, 5] were implemented in Python. The Nelder–Mead Simplex algorithm [21], available in the Scipy Python library, was employed to optimize the parameters. Only the hysteretic parameters were adjusted, while the envelope parameters were kept fixed. An inverse process was also used to determine the initial values for all parameters. The following multi-linear function $\epsilon(\mathbf{p})$ was used to obtain the optimal model parameters $\hat{\mathbf{p}}$

$$\epsilon(\mathbf{p}) = 0.5\eta_{F,\text{nrms}} + 0.5\eta_{\Upsilon,\text{nrms}}, \tag{1}$$

where $\eta_{F,\text{nrms}}$ is the Normalized Root Mean Square (NRMS) error for the force history $F(t)$, and $\eta_{\Upsilon,\text{nrms}}$ is the NRMS error for the dissipated energy $\Upsilon(t)$ one. For a generic estimator $\hat{\mathbf{y}}$ of the measured variable $\mathbf{y}$, the NRMS error is defined as

$$\eta_{\text{nrms}} = \frac{1}{\Delta y}\sqrt{\frac{1}{n}\sum_{i=1}^{n}(y_i - \hat{y}_i)^2}, \tag{2}$$

where y_i and $\hat{y}_i$ are the respective i-th sample, with $i < n$, and $\Delta y = y_{\text{max}} - y_{\text{min}}$. A maximum of 100 evaluations and 200 iterations were used to stop the optimization process. The parameters obtained for all models are listed in the tables of Appendix A.

3.3 MODELS RESPONSE

Fig. 3 illustrates the force–displacement $F(u)$ hysteresis for the four models evaluated in the benchmark tests. Overall, the ASPID model best fits all cases, followed by the DowelType and MRA models. Additionally, it highlights some important observations.

First, the most challenging task across all specimens is predicting the strength and stiffness during the pinching phase of the UR paths. All models offer different approximations tailored to the specific specimen. Moreover, specimen S4 presents an additional challenge due to the need to replicate the strength and stiffness asymmetry of UR paths, while specimen S3 adds complexity by requiring accurate reproduction of the trailing cycles —i.e., secondary cycles that exhibit reduced amplitude compared to the primary ones. Some over- and underestimations of pinching branches have been noted for specimens S1, S2, and S4 when using the SAWS, MRA, and DowelType models. Second, the P/N envelopes for specimens S1, S2, and S4 are accurately simulated by all models. Moreover, all models except the SAWS model can effectively simulate the asymmetric P/N envelopes of specimen S3. Third, the

Table 2: *Summary of benchmark tests simulated.*

				Load		
Authors	**Id**	**Specimen**	**Member**	***Direction***	***Type***	**Behavior**
Gavrić et al. 2015 [15]	S1	19-CS-05	CLT joint	Shear	Cyclic	Symmetric
Orellana et al. 2016 [23]	S2	T8-120CL50-02	LFT wall	Shear	Cyclic	Disp. asym.
Carrero et al. 2020 [3]	S3	CLT-RCwo	Hybrid timber-concrete joint	Shear	Cyclic	Force asym.
Gavrić et al. 2015 [15]	S4	1-CN-05	Hold-down CLT joint	Axial	Load-reversal	Taxonomical asym.

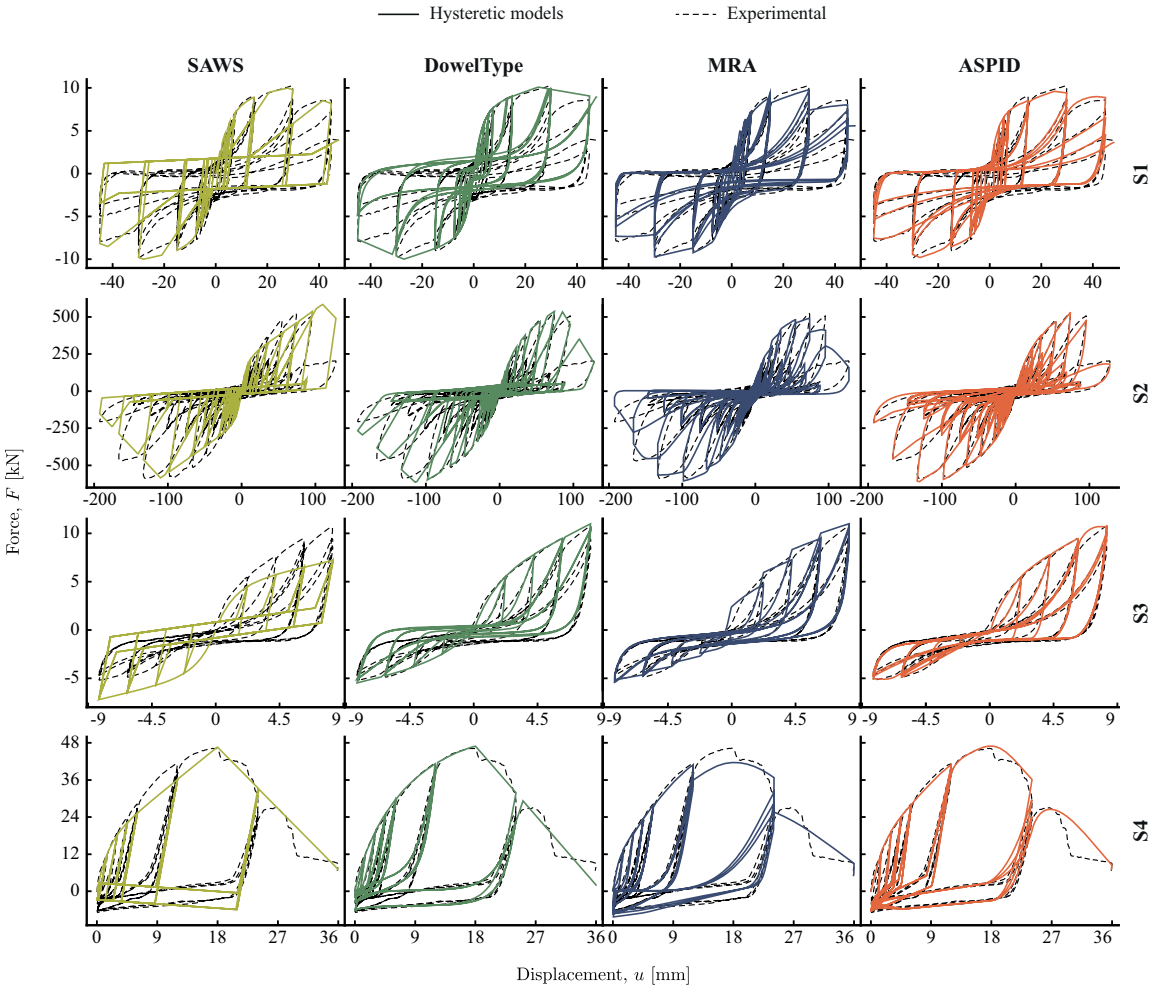

Figure 3: *Comparison of force–displacement $F(u)$ hysteresis among all models and benchmarks.*

UR paths of all specimens are simulated more accurately with the DowelType, MRA, and ASPID models compared to the SAWS model. This is because the former models produce nonlinear smooth shapes, while the SAWS model produces polygonal shapes. Consequently, this difference affects the accuracy of span displacement in the pinching branches. Notable overestimations in the positive pinching phase have been observed in specimens S1 and S3 using the SAWS and DowelType models, and in specimen S4 using the MRA model. Nevertheless, the assumption about constant unloading stiffness is valid for all specimens and models. Fourth, the pinching ordinate translation (down- or up-shifting) in both loading directions is evident in the ASPID, MRA, and DowelType models, depending on the specimen; some of which agree with the test results, while others do not. In the DowelType model, assigning a single initial value for the P/N branches can lead to significant inaccuracies for specimens S1 and S3. The MRA model allows for two different initial values for the P/N branches but does not control the direction and increment, which leads to errors in specimen S2. In contrast, the ASPID model can independently control the initial position, direction, and increments of each loading direction, resulting in greater accuracy across the board. On the other hand, the SAWS model maintains a constant, unique value for the P/N directions, causing inaccuracies in specimens S1 and S2. Fifth, the transition phase is difficult to simulate accurately with the SAWS, MRA, and DowelType models, while the ASPID model fits this phase well due to its specific feature for this purpose. This transition phase is more pronounced in specimens S1 and S2, mainly when greater strength is degraded.

Fig. 4 shows the normalized history of dissipated energy $\Upsilon(t/T)/\Upsilon_{te}$ for the four models across all tests, where Υ_{te} refers to the total dissipated energy measured during the experiment and T indicates the duration of the pseudo-time. All models demonstrate a good fit across the tests. However, minor discrepancies were noted in specimens S1 and S3 for the SAWS model and specimens S4 for the MRA model.

3.4 EPISTEMIC UNCERTAINTY QUANTIFICATION

To assess the epistemic uncertainty of hysteretic models, three mechanical parameters were calculated: (i) peak force F_{max}; (ii) displacement at peak force u_{max}; and (iii) total dissipated energy Υ_t. In addition, three dimensionless Goodness-of-Fit (GoF) metrics for the force $F(t)$ and the

https://doi.org/10.52202/080513-0179

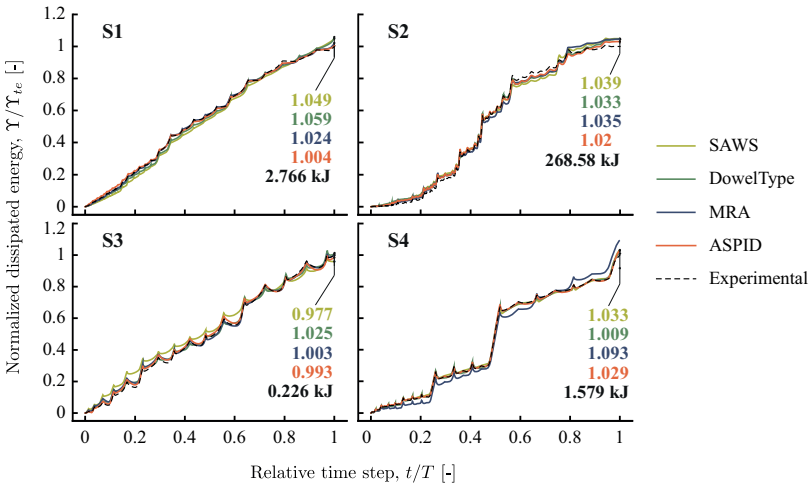

Figure 4: *Comparison of normalized dissipated energy–relative time step $\Upsilon(t/T)/\Upsilon_{te}$ for the four models in the benchmark tests. This includes the total dissipated energy value of each experiment Υ_{te}, and the corresponding model/test ratio.*

dissipated energy histories $\Upsilon(t)$ were evaluated: (i) the NRMS error η_{nrms} (defined in Equation 2); (ii) the Normalized Mean Absolute (NMA) error η_{nma}; and (iii) the coefficient of determination η_{det} (R^2-factor). The last two metrics are defined, respectively, as

$$\eta_{\text{nma}} = \frac{1}{n\Delta y}\sum_{i=1}^{n}|y_i - \hat{y}_i|, \tag{3a}$$

$$\eta_{\text{det}} = 1 - \frac{\sum_{i=1}^{n}(y_i - \hat{y}_i)^2}{\sum_{i=1}^{n}(y_i - \bar{y})^2}, \tag{3b}$$

where $\bar{y}$ is the mean of the measured variable $\mathbf{y}$. Fig. 5 presents a boxplot summarizing the uncertainty in the three mechanical parameters (F_{max}, u_{max}, Υ_t), with variations based on the specimen and the hysteretic model employed. The force and corresponding displacements are included in the statistics for both P/N values. Furthermore, Table 3 outlines the three GoF metrics for the force and dissipated energy histories. When comparing each specimen across all models (see Fig. 5a), the predictions for the three parameters are generally satisfactory, with a mean error of up to 7% and a Coefficient of Variation (CoV) of less than 6.43%. However, exceptions include the peak force for specimen S3 and the respective displacement for specimen S2, which exhibit a CoV exceeding 17%. In analyzing each model across all specimens (refer to Fig. 5b), the estimates for all parameters in the DowelType, MRA, and ASPID model are reliable, yielding a mean error of up to 4% and a CoV of less than 9.45%. In contrast, the SAWS model displays moderate uncertainty, with a CoV greater than 18% for the parameters F_{max} and u_{max}. Notably, the lowest uncertainty is observed in the total dissipated energy Υ_t, which has a CoV of less than 3.21% and an error of up to 9.3% when compared to experimental results (see Fig. 4).

The results indicated that the two GoF error metrics for all cases were below 8.54% and 4.43% for the force and dissipated energy history, respectively. Furthermore, the R^2 values for the force history ranged 83.11–99.03%, while those for the dissipated energy history ranged 97.92–99.96%. In every case, the GoF error metrics for the dissipated energy history were smaller than those for the force history, and the R^2-factor was higher for the dissipated energy history than the force history. This suggests that the parameter identification process effectively fitted both the force and dissipated energy histories for all models and tests, except for specimen S3 using the SAWS model, which encountered difficulties. Overall, the adjustments for the dissipated energy history curves were more precise than those for the force history.

The ranking of the GoF metrics for the force hysteresis is led by the ASPID model, which consistently exhibits more minor errors for η_{nrms} and η_{nma}, along with higher values of η_{det} compared to the other models. Depending on the specific specimen, the DowelType and MRA models share the second and third positions. The SAWS model usually occupies the fourth position. Regarding dissipated energy, the ASPID, MRA, and DowelType models frequently occupy the top three positions, with their rankings varying depending on the specimens and the metric used. Conversely, in nearly all cases, the SAWS model finishes last.

4 – SUMMARY AND CONCLUSIONS

This study compared the hysteretic response of four phenomenological-based timber models found in the literature using four experimental benchmark tests on timber. The models evaluated were: (i) SAWS or MSTEW; (ii) DowelType; (iii) Modified Richard–Abbott (MRA), an improved version created by the authors; and (iv) ASPID, a new proposed model by the authors. Three mechanical parameters were compared: strength capacity, displacement at peak strength, and energy dissipation. Additionally, three goodness-of-fit metrics for the force and energy dissipation history were analyzed: the normalized root mean square error η_{NRMS}, normalized mean absolute error η_{NMA}, and coefficient of determination R^2. The main results are:

- The four models simulate the force–displacement hysteresis from benchmark tests with varying levels of approximation concerning the specific mechanical parameter measured. All models successfully replicate

Table 3: *Goodness-of-fit comparison of the four hysteretic models in benchmark tests.*

	η_{nrms} [%]				η_{nma} [%]				η_{det} [%]			
Specimen	***SAWS***	***DT****	***MRA***	***ASPID***	***SAWS***	***DT***	***MRA***	***ASPID***	***SAWS***	***DT***	***MRA***	***ASPID***
Force, $F(t)$												
S1	5.74	5.90	3.79	2.98	4.66	4.81	2.75	2.08	88.24	87.39	95.13	97.00
S2	5.17	4.17	4.41	2.29	3.29	3.11	3.26	1.67	83.55	89.61	89.51	96.94
S3	8.54	4.49	2.81	1.85	7.19	3.89	1.92	1.33	83.11	93.91	97.63	99.03
S4	6.03	4.02	6.06	3.94	4.80	3.13	4.04	2.48	93.57	97.08	94.13	97.17
Dissipated energy, $\Upsilon(t)$												
S1	2.64	1.64	1.25	1.32	2.38	1.39	0.47	0.62	99.22	99.69	99.83	99.82
S2	2.86	2.05	2.64	2.05	2.44	1.74	2.04	1.49	99.38	99.69	99.48	99.70
S3	4.43	1.50	1.58	1.46	3.83	1.27	1.05	1.11	97.92	99.74	99.72	99.77
S4	0.91	0.66	3.58	1.61	0.71	0.56	2.82	0.39	99.91	99.96	98.45	99.72

* DT: DowelType.

the Unloading–Reloading (UR) paths, the pinching effect, and the degradation of strength and stiffness. Notably, the DowelType, MRA, and ASPID models effectively simulate asymmetric envelopes and UR paths, while both the ASPID and MRA models represent the effects of low-cycle fatigue. The most challenging aspect of fitting the UR paths occurs in the pinching zone, which is characterized by near-zero displacement, resulting in greater variability among the models.

- Numerical simulations of all benchmarks effectively predicted the peak force and total dissipated energy with a mean error of up to 7% (excluding the SAWS model). The DowelType, MRA, and ASPID models demonstrated high accuracy in estimating all mechanical parameters, achieving a mean error of less than 4% and a coefficient of variation of less than 9.45%. All models also successfully predicted the total dissipated energy Υ_t, with an error of less than 9.3%. Furthermore, the η_{NRMS} and η_{NMA} errors for the force and dissipated energy history were both under 8.54% and 4.43%, respectively. In contrast, the R^2 values for the force and energy histories range 83.11–99.03% and 97.9–99.96%, respectively. Generally, the energy dissipation history aligns more closely with the data than the force history does.

ACKNOWLEDGEMENTS

This article was funded by the Centro Nacional de Excelencia para la Industria de la Madera (CENAMAD), ANID/BASAL/FB210015. Thanks to Igor Gavrić, Tulio Carrero, and Paul Orellana for providing the data for the experimental benchmark tests.

5 – APPENDIX A. OPTIMIZED PARAMETERS FOR ALL HYSTERETIC MODELS

Tables 4–7 present the optimized parameters for the four hysteretic timber models used in the benchmark tests. Each table categorizes the parameters into hysteretic and envelope types. The hysteretic parameters are optimized using the algorithm described in Section 3, while the envelope parameters are determined through the classical inverse process.

For detailed information regarding the parameters of the SAWS and DowelType models, please refer to `www.openseespydoc.readthedocs.io/en/latest/src/SAWS.html` and `www.opensees.github.io/OpenSeesDocumentation/user/manual/material/uniaxialMaterials/DowelType.html`, respectively. For the meaning of the parameters for the MRA and ASPID models, please consult [4, 6], respectively.

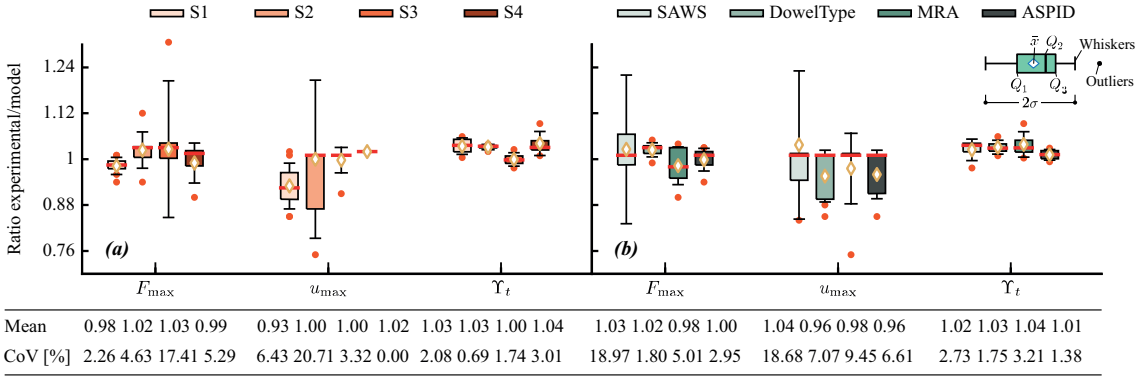

Figure 5: *Boxplot of three mechanical parameters ($F_{\max}$, $u_{\max}$, and Υ_t) for the four hysteretic models in benchmark tests: (a) variability for each specimen and (b) variability across models.*

https://doi.org/10.52202/080513-0179

Table 4: *Parameters for the SAWS model used in the benchmark tests.*

		Specimen			
Parameter	**Unit**	***S1***	***S2***	***S3***	***S4***
Hysteretics					
R_3	–	1.531	0.992	2.021	1.082
R_4	–	0.007	0.010	0.052	-0.014
α	–	0.942	0.470	0.021	0.014
β	–	1.392	1.055	1.006	1.007
F_I	kN	1.770	20.393	0.815	2.696
Envelopes					
S_0	kN/mm	1.8	35	4	11
F_0	kN	8.5	200	4.4	15
R_1	–	0.03	0.1	0.085	0.16
R_2	–	-0.06	-0.15	-0.1	-0.2
D_U	mm	28	110	20	18

REFERENCES

[1] A. Aloisio, R. Alaggio, J. Köhler, and M. Fragiacomo. "Extension of Generalized Bouc-Wen Hysteresis Modeling of Wood Joints and Structural Systems." In: *Journal of Engineering Mechanics* 146.3 (2020), p. 04020001. DOI: 10.1061/(ASCE)EM.1943-7889.0001722.

[2] F. Ávila, P. Dechent, and A. Opazo. "Seismic behaviour evaluation of CLT horizontal diaphragms on hybrid buildings with reinforced concrete shear walls." In: *Engineering Structures* 244 (2021), p. 112698. DOI: 10.1016/j.engstruct.2021.112698.

[3] T. Carrero, J. Montaño, H. Santa-María, and P. Guindos. "Static and dynamic performance of direct hybrid connections of cross-laminated timber with steel, concrete and laminated strand lumber composites." In: *Latin American Journal of Solids and Structures* 17.4 (2020). DOI: dx.doi.org/10.1590/1679-78256106.

[4] M. F. Chacón and P. Guindos. "ASPID: An asymmetric pinching damaged hysteresis model for timber structures." In: *Construction and Building Materials* 404 (2023), p. 133106. DOI: 10.1016/j.conbuildmat.2023.133106.

[5] M. F. Chacón and P. Guindos. "P2PE: A finite element formulation for panel-to-panel cross-laminated timber connections." In: *Computers and Structures* 300 (2024), p. 107404. DOI: 10.1016/j.compstruc.2024.107404.

[6] M. F. Chacón, A. Jara-Cisterna, F. Benedetti, F. Véliz, and P. Guindos. "In-plane testing and hysteretic modeling of steel-spline cross-laminated timber diaphragm connection with self-tapping screws." In: *Wood Material Science & Engineering* (2024). DOI: 10.1080/17480272.2024.2358145.

[7] H. Dong, M. He, X. Wang, C. Christopoulos, Z. Li, and Z. Shu. "Development of a uniaxial hysteretic model for dowel-type timber joints in OpenSees." In: *Construction and Building Materials* 288 (2021), p. 123112. DOI: 10.1016/j.conbuildmat.2021.123112.

[8] X. Estrella, P. Guindos, J. L. Almazán, and S. Malek. "Efficient nonlinear modeling of strong wood frame shear walls for mid-rise buildings." In: *Engineering Structures* 215 (2020), p. 110670. DOI: 10.1016/j.engstruct.2020.110670.

[9] G. C. Foliente. "Hysteresis Modeling of Wood Joints and Structural Systems." In: *Journal of Structural Engineering* 121.6 (1995), pp. 1013–1022. DOI: 10.1061/(ASCE)0733-9445(1995)121:6(1013).

[10] B. Folz and A. Filiatrault. "Cyclic Analysis of Wood Shear Walls." In: *Journal of Structural Engineering* 127.4 (2001), pp. 433–441. DOI: 10.1061/(ASCE)0733-9445(2001)127:4(433).

[11] R. O. Foschi. "Modeling the hysteretic response of mechanical connections for wood structures." In: *Proceddings of the 2nd World Conference on Timber Engineering*. Whistler, Canada, 2000.

[12] F. N. Fritsch and J. Butland. "A method for constructing local monotone piecewise cubic interpolants." In: *SIAM Journal on Scientific and Statistical Computing* 5.2 (1984), pp. 300–304. DOI: doi.org/10.1137/0905021.

[13] I. Gavrić, M. Fragiacomo, and A. Ceccotti. "Cyclic Behavior of CLT Wall Systems: Experimental Tests and Analytical Prediction Models." In: *Journal of Structural Engineering* 141.11 (2015), p. 04015034. DOI: 10.1061/(ASCE)ST.1943-541X.0001246.

[14] I. Gavrić, M. Fragiacomo, and A. Ceccotti. "Cyclic behaviour of typical metal connectors for cross-laminated (CLT) structures." In: *Materials and Structures* 48 (2015), pp. 1841–1857. DOI: 10.1617/s11527-014-0278-7.

[15] I. Gavrić, M. Fragiacomo, and A. Ceccotti. "Strength and Deformation Characteristics of Typical X-Lam Connections." In: *Proceedings of the 8th World Conference on Timber Engineering*. Auckland, New Zealand, 2012.

[16] T. Han and S. Tesfamariam. "Numerical analysis of CLT shear walls using high-fidelity model: Connection to building system." In: *Journal of Building Engineering* 72 (2023), p. 106458. DOI: 10.1016/j.jobe.2023.106458.

[17] A. Hossain, M. Popovski, and T. Tannert. "Cross-laminated timber connections assembled with a combination of screws in withdrawal and screws in shear." In: *Engineering Structures* 168 (2018), pp. 1–11. DOI: 10.1016/j.engstruct.2018.04.052.

[18] A. Iqbal, M. Fragiacomo, S. Pampanin, and A. Buchanan. "Seismic resilience of plywood-coupled LVL wall panels." In: *Engineering Structures* 167 (2018), pp. 750–759. DOI: 10.1016/j.engstruct.2017.09.053.

Table 5: *Parameters for the DowelType model used in the benchmark tests.*

		Specimen			
Parameter	**Unit**	***S1***	***S2***	***S3***	***S4***
Hysteretics					
F_i	kN	1.498	25.784	0.097	4.982
K_p	kN/mm	0.062	1.227	0.103	0.907
R_u	–	8.461	3.622	6.766	1.738
c	–	1.024	0.242	0.871	1.084
β	–	0.729	1.276	1.017	1.028
γ	–	1.551	0.856	1.081	1.037
η	–	0.516	0.068	0.196	0.104
D_y	mm	14.873	39.527	3.997	17.387
α_p	–	1.160	0.935	1.148	9.772
α_u	–	1.024	1.487	1.110	1.025
α_r	–	1.492	1.113	0.414	1.063
Envelopes					
Curve		Exponential	Exponential	Exponential	Bézier
$K_0^{\pm}$	kN	[2.6, 2.6][a]	[20, 20]	[4.0, 1.5]	–
$R_1^{\pm}$	–	[1/25, 1/25]	[1/7, 1/7]	[1/5.5, 1/5]	–
$F_0^{\pm}$	kN	[7.5, -7.2]	[33, -32]	[5.0, -3.1]	–
$D_c^{\pm}$	mm	[25, -27]	[82, -110]	[10, -10]	–
$K_d^{\pm}$	kN/mm	[2.6/50, 2.6/20]	[20/2.5, 20/4.5]	[2.6/50, 2.6/20]	–
$D_u^{\pm}$	mm	[50, -50]	[300, -300]	[10, -20]	–
$Db_1^{\pm}$	mm	–	–	–	[2, -2]
$Fb_1^{\pm}$	kN	–	-	–	[20, -20]
$Db_2^{\pm}$	mm	–	–	–	[7, -7]
$Fb_2^{\pm}$	kN	–	–	–	[40, -40]
$D_c^{\pm}$	mm	–	–	–	[18, -18]
$F_c^{\pm}$	kN	–	–	–	[47, -47]
$K_d^{\pm}$	kN/mm	–	–	–	[2.5, 2.5]
$D_u^{\pm}$	mm	–	–	–	[60, -60]

[a] Values between brackets correspond to the positive (left) and negative (right) loading direction, respectively.

Table 6: *Parameters for the MRA model used in the benchmark tests.*

		Specimen			
Parameter	**Unit**	***S1***	***S2***	***S3***	***S4***
Hysteretics					
$\overset{*}{K}_{ho}^{\pm}$	kN/mm	[0.276, 0.265 0.062, 0.069][a]	[7.435, 8.111 3.243, 3.492]	[0.906, 0.333 0.101, 0.101]	[4.972, 0.728 0.043, 1.069]
$\overset{*}{m}^{\pm}$	–	[3.833, 3.959, 3.859, 3.998]	[1.984, 1.607, 2.032, 2.097]	[1.980, 1.498, 1.450, 1.310]	[3.771, 4.148, 3.787, 4.514]
$t_1^{\pm}$	–	(41.066, 34.882)[b]	(36.316, 22.930)	(26.909, 25.508)	(15.161, 20.425)
$t_2^{\pm}$	–	(0.102, 0.102)	(0.336, 0.186)	(0.303, 0.406)	(0.265, 0.106)
$t_3^{\pm}$	–	(1.022, 1.024)	(0.944, 0.969)	(1.050, 0.988)	(1.042, 0.777)
J_f	–	5.613×10^{-7}	3.162×10^{-9}	7.062×10^{-7}	2.431×10^{-7}
J_k	–	1.021×10^{-8}	4.009×10^{-9}	1.002×10^{-7}	5.736×10^{-7}
Envelopes					
$\overset{*}{K}_o^{\pm}$	kN/mm	[1, 1, 3, 3]	[20, 22, 28, 20]	[1, 4, 6, 25]	[10, 10, 20, 15]
$\overset{*}{F}_o^{\pm}$	kN	[7, 6, 0.5, 3]	[20, 40, 10, 50]	[5, 2, -1, 1]	[10, 1, 0.1, -3]
$\overset{*}{r}_1^{\pm}$	–	[5, 5, 5, 5]	[90, 80, 20, 20]	[15, 13, 5, 5]	[15, 15, 5, 5]
$\overset{*}{r}_2^{\pm}$	–	[0.01, 0.01, 0.01, 0.01]	[5×10^{-4}, 0.002, 0.1, 0.1]	[0.01, 0.01, 0.01, 0.01]	[0.002, 0.01, 0.01, 0.01]
$\overset{*}{r}_3^{\pm}$	–	[-1/20, -1/20, -1/20, -1/20]	[-1/20, -1/20, -1/20, -1/20]	[1, 1, 1, 1]	[-1/2, -1/20, -1/20, -1/20]

[a] Values between brackets correspond to the P/N upper (first two) and P/N lower (last two) parameters.
[b] Values between parentheses correspond to the respective positive (left) and negative (right) ones.

[19] M. Izzi, G. Rinaldin, M. Fragiacomo, and A. Polastri. "Numerical modelling of steel-to-timber joints and connectors for CLT structures." In: *Proceddings of the 10th World Conference on Timber Engineering, Vienna, Austria*. 2016.

https://doi.org/10.52202/080513-0179

Table 7: *Parameters for the ASPID model used in the benchmark tests.*

		Specimen			
Parameter	**Unit**	***S1***	***S2***	***S3***	***S4***
Hysteretics					
$f_{po}^{\pm}$	kN	[1.172, -2.999][a]	[7.840, -23.943]	[-0.362, -1.001]	[-3.457, -6.484]
$K_{po}^{\pm}$	kN/mm	[0.157, 0.153]	[7.885, 6.648]	[0.310, 0.109]	[3.011, 3.948]
$K_{ro}^{\pm}$	kN/mm	[6.102, 5.985]	[41.266, 37.092]	[6.629, 1.424]	[10.125, 49.975]
$K_{u}^{\pm}$	kN/mm	[7.635, 6.769]	[78.659, 89.144]	[8.436, 20.355]	[19.943, 14.147]
$\lambda_{r}^{\pm}$	–	[0.450, 0.657]	[0.255, 0.359]	[0.413, 0.506]	[0.311, 0.200]
$\lambda_{u}^{\pm}$	–	[0.083, 0.119]	[0.194, 0.137]	[0.137, 0.161]	[0.396, 0.248]
$\lambda_{t}^{\pm}$	–	[0.202, 0.200]	[0.189, 0.187]	[0.197, 0.101]	[0.299, 0.198]
$A_{p}^{\pm}$	–	[0.065, 0.068]	[0.018, 0.016]	[0.044, 0.109]	[0.092, 0.121]
$A_{r}^{\pm}$	–	[0.074, 0.080]	[0.018, 0.020]	[0.040, 0.065]	[0.010, 0.001]
$A_{o}^{\pm}$	–	[-0.010, 0.030]	[0.010, -0.001]	[0.096, -0.052]	[0.010, -0.010]
B_{u}	–	6.384×10^{-5}	5.540×10^{-6}	1.614×10^{-4}	2.029×10^{-4}
B_{e}	–	3.169×10^{-4}	2.679×10^{-6}	5.504×10^{-2}	1.003×10^{-3}
Envelopes					
Curve, $G_{e}^{\pm}(x)$[b]	–	[III, III]	[IV, IV]	[III, III]	[II[c], N]
$K_{o}^{\pm}$	kN/mm	[2.6, 2.6]	[20, 20]	[4, 0.9]	[–, 5]
$g_{o}^{\pm}$	kN	[7,7]	[330,320]	[5, 10]	[–, –]
$r_{1}^{\pm}$	–	[1/25, 1/25]	[1/7, 1/7]	[1/5.5, 1/4]	[–, –]
$r_{2}^{\pm}$	–	[-1/70, -1/20]	[–, –]	[-1/7, -1/15]	[–, –]
$r_{3}^{\pm}$	–	[-0.02, -0.02]	[–, –]	[-0.02, -0.02]	[–, –]
$x_{p}^{\pm}$	mm	[25, 27]	[95, 90]	[8.1, 6.6]	[–, –]
$x_{s}^{\pm}$	mm	[45, 50]	[155, 320]	[10, 18]	[–, –]

[a] Values between brackets correspond to the positive (left) and negative (right) loading direction, respectively.
[b] N: linear-elastic; I: linear interpolation; II: monotone cubic-spline interpolation given by [12]; III: exponential-linear relation given by [4]; and IV: exponential-cubic relation given by [4].
[c] Control points: $\mathbb{X}^{+} = \{[0, 0], [2, 15], [6, 28], [15, 45], [18, 47], [25, 34], [38, 3]\}$.

[20] F. McKenna, G. L. Fenves, and M. H. Scott. *Open system for earthquake engineering simulation*. University of California. Berkeley, CA, USA, 2024.

[21] J. Nelder and R. Mead. "A Simplex Method for Function Minimization." In: *The Computer Journal* 7.4 (1965), pp. 308–313. DOI: 10.1093/comjnl/7.4.308.

[22] P. Nogueiro, L. S. da Silva, R. Bento, and R. Simões. "Numerical implementation and calibration of a hysteretic model with pinching for the cyclic response of steel joints." In: *Proceddings of the 4th International Conference on Advances in Steel Structures*. Shanghai, China, 2005, pp. 767–774. DOI: 10.1016/B978-008044637-0/50112-8.

[23] P. Orellana, H. Santa María, J. L. Almazan, and X. Estrella. "Cyclic behavior of wood-frame shear walls with vertical load and bending moment for mid-rise timber buildings." In: *Engineering Structures* 240 (2021), p. 112298. DOI: 10.1016/j.engstruct.2021.112298.

[24] W. C. Pang, D. Rosowsky, S. Pei, and J. W. van de Lindt. "Evolutionary Parameter Hysteretic Model for Wood Shear Walls." In: *Journal of Structural Engineering* 133.8 (2007), pp. 1118–1129. DOI: 10.1061/(ASCE)0733-9445(2007)133:8(1118).

[25] S. Pei and J. W. van de Lindt. "Coupled shear-bending formulation for seismic analysis of stacked wood shear wall systems." In: *Earthquake Engineering & Structural Dynamics* 38 (2009), pp. 1631–1647. DOI: 10.1002/eqe.926.

[26] T. Ray and A. M. Reinhorn. "Enhanced Smooth Hysteretic Model with Degrading Properties." In: *Journal of Structural Engineering* 140.1 (2014), p. 04013028. DOI: 10.1061/(ASCE)ST.1943-541X.0000798.

[27] N. Richard, L. Daudeville, H. Prion, and F. Lam. "Timber shear walls with large openings: experimental and numerical prediction of the structural behaviour." In: *Canada Journal of Civil Engineering* 29 (2002), pp. 713–724. DOI: 10.1139/L02-050.

[28] R. M. Richard and B. J. Abbott. "Versatile Elastic-Plastic Stress-Strain Formula." In: *Journal of the Engineering Mechanics Division* 101.4 (1975), pp. 511–515. DOI: doi.org/10.1061/JMCEA3.0002047.

[29] W. G. Stewart. "The Seismic Design of Plywood Sheated Shear Walls." PhD thesis. Christchurch, New Zealand: University of Canterbury, 1987.

[30] K. Sullivan, T. H. Miller, and R. Gupta. "Behavior of cross-laminated timber diaphragm connections with self-tapping screws." In: *Engineering Structures* 168 (2018), pp. 505–524. DOI: 10.1016/j.engstruct.2018.04.094.